



AFRL-RX-WP-JA-2017-0509

**FATIGUE CRACK GROWTH AND FRACTURE
BEHAVIOR OF AS-CAST Ti-43.5AL-4Nb-1Mo-0.1B
(TNM) COMPARED TO Ti-48AL-2Nb-2Cr (4822)
(POSTPRINT)**

Matthew S. Dahara and John J. Lewandowskia

Case Western Reserve University

Sesh A. Tamirisakandala

Arconic Titanium & Engineered Products

**22 November 2017
Interim Report**

**Distribution Statement A.
Approved for public release: distribution unlimited.**

© ELSEVIER LTD

(STINFO COPY)

**AIR FORCE RESEARCH LABORATORY
MATERIALS AND MANUFACTURING DIRECTORATE
WRIGHT-PATTERSON AIR FORCE BASE, OH 45433-7750
AIR FORCE MATERIEL COMMAND
UNITED STATES AIR FORCE**

REPORT DOCUMENTATION PAGE				<i>Form Approved</i> OMB No. 0704-0188	
The public reporting burden for this collection of information is estimated to average 1 hour per response, including the time for reviewing instructions, searching existing data sources, gathering and maintaining the data needed, and completing and reviewing the collection of information. Send comments regarding this burden estimate or any other aspect of this collection of information, including suggestions for reducing this burden, to Department of Defense, Washington Headquarters Services, Directorate for Information Operations and Reports (0704-0188), 1215 Jefferson Davis Highway, Suite 1204, Arlington, VA 22202-4302. Respondents should be aware that notwithstanding any other provision of law, no person shall be subject to any penalty for failing to comply with a collection of information if it does not display a currently valid OMB control number. PLEASE DO NOT RETURN YOUR FORM TO THE ABOVE ADDRESS.					
1. REPORT DATE (DD-MM-YY) 22 November 2017		2. REPORT TYPE Interim		3. DATES COVERED (From - To) 25 January 2007 – 22 October 2017	
4. TITLE AND SUBTITLE FATIGUE CRACK GROWTH AND FRACTURE BEHAVIOR OF AS-CAST Ti-43.5Al-4Nb-1Mo-0.1B (TNM) COMPARED TO Ti-48Al-2Nb-2Cr (4822) (POSTPRINT)				5a. CONTRACT NUMBER FA8650-06-2-5211	
				5b. GRANT NUMBER	
				5c. PROGRAM ELEMENT NUMBER 62102F	
6. AUTHOR(S) 1) Matthew S. Dahara and John J. Lewandowskia – CWRU 2) Sesh A. Tamirisakandala – ATEP				5d. PROJECT NUMBER 2241	
				5e. TASK NUMBER	
				5f. WORK UNIT NUMBER X02N	
7. PERFORMING ORGANIZATION NAME(S) AND ADDRESS(ES) 1) Case Western Reserve University 10900 Euclid Ave. Cleveland, OH 44106 2) Arconic Titanium & Engineered Products 1000 Warren Ave. Niles, OH 44446				8. PERFORMING ORGANIZATION REPORT NUMBER	
9. SPONSORING/MONITORING AGENCY NAME(S) AND ADDRESS(ES) Air Force Research Laboratory Materials and Manufacturing Directorate Wright-Patterson Air Force Base, OH 45433-7750 Air Force Materiel Command United States Air Force				10. SPONSORING/MONITORING AGENCY ACRONYM(S) AFRL/RXCM	
				11. SPONSORING/MONITORING AGENCY REPORT NUMBER(S) AFRL-RX-WP-JA-2017-0509	
12. DISTRIBUTION/AVAILABILITY STATEMENT Distribution Statement A. Approved for public release; distribution unlimited.					
13. SUPPLEMENTARY NOTES PA Case Number: 88ABW-2017-5879; Clearance Date: 22 Nov 2017. This document contains color. Journal article published in Intermetallics, Vol. 91, 17 Sep 2017. © 2017 Elsevier Ltd. The U.S. Government is joint author of the work and has the right to use, modify, reproduce, release, perform, display, or disclose the work. The final publication is available at www.elsevier.com/locate/internet http://dx.doi.org/10.1016/j.intermet.2017.08.015					
14. ABSTRACT (Maximum 200 words) The effects of sample orientation and load ratio on the room-temperature fatigue crack growth and fracture behavior of a third-generation gamma titanium aluminide Ti-43.5Al-4Nb-1Mo-0.1B (TNM) were determined and compared with that of a second-generation alloy Ti-48Al-2Nb-2Cr (4822). Both materials are currently used as low pressure turbine blades in fuel-efficient gas turbine engines. Bend bar specimens, excised from the as-cast articles in the longitudinal and transverse directions to the casting direction, were tested at room temperature in lab air. Load ratios in the range 0.1–0.9 were used in fatigue testing to determine their effects on the fatigue threshold, Paris law slope, and stress intensity at overload in fatigue. Microscopy and fractography were used to document the effects of sample orientation on the fatigue crack path and morphology. Significant effects of changes in load ratio were observed on the fatigue threshold and Paris law slope, while effects of sample orientation were minimal for both alloys. The effects of microstructure length scale and differences in microconstituents are discussed in relation to the properties measured.					
15. SUBJECT TERMS fatigue crack; gamma titanium aluminide Ti-43; low pressure turbine blades; turbine engines; fatigue testing; fractography					
16. SECURITY CLASSIFICATION OF:			17. LIMITATION OF ABSTRACT: SAR	18. NUMBER OF PAGES 13	19a. NAME OF RESPONSIBLE PERSON (Monitor) Micheal Burba 19b. TELEPHONE NUMBER (Include Area Code) (937) 255-9795
a. REPORT Unclassified	b. ABSTRACT Unclassified	c. THIS PAGE Unclassified			



Fatigue crack growth and fracture behavior of as-cast Ti-43.5Al-4Nb-1Mo-0.1B (TNM) compared to Ti-48Al-2Nb-2Cr (4822)



Matthew S. Dahar^{a,*}, Sesh A. Tamirisakandala^b, John J. Lewandowski^a

^a Case Western Reserve University, Department of Materials Science and Engineering, Cleveland, OH 44106, USA

^b Arconic Titanium & Engineered Products, Niles, OH 44446, USA

ABSTRACT

The effects of sample orientation and load ratio on the room-temperature fatigue crack growth and fracture behavior of a third-generation gamma titanium aluminide Ti-43.5Al-4Nb-1Mo-0.1B (TNM) were determined and compared with that of a second-generation alloy Ti-48Al-2Nb-2Cr (4822). Both materials are currently used as low pressure turbine blades in fuel-efficient gas turbine engines. Bend bar specimens, excised from the as-cast articles in the longitudinal and transverse directions to the casting direction, were tested at room temperature in lab air. Load ratios in the range 0.1–0.9 were used in fatigue testing to determine their effects on the fatigue threshold, Paris law slope, and stress intensity at overload in fatigue. Microscopy and fractography were used to document the effects of sample orientation on the fatigue crack path and morphology. Significant effects of changes in load ratio were observed on the fatigue threshold and Paris law slope, while effects of sample orientation were minimal for both alloys. The effects of microstructure length scale and differences in microconstituents are discussed in relation to the properties measured.

1. Introduction

Gamma titanium aluminides consisting of γ -TiAl (ordered face-centered tetragonal L1₀ structure) plus α_2 -Ti₃Al (ordered hexagonal DO₁₉ structure) phases have emerged as promising candidates with attractive mechanical properties (e.g. tensile and creep strength) as a replacement for heavy nickel-based superalloys for intermediate-temperature applications such as low pressure turbine (LPT) blades of fuel-efficient jet engines [1,2]. The second generation alloy compositions can be generalized as: Ti-(45–48)Al – (1–3)X1 – (2–5)Y1 – (< 1)Z1, where X1 = Cr, Mn, V; Y1 = Nb, Ta, W, Mo; Z1 = Si, B, C (all compositions expressed in atomic percent). Ti-48Al-2Cr-2Nb (4822) is a second generation alloy that has been in service since 2011 on GEnx™ engine LPT cast blades. Third generation alloy compositions can be represented as: Ti-(42–45)Al – (0–10)X2 – (0–3)Y2 – (0–1)Z2 – (0–0.5)RE, where X2 = Cr, Mn, Nb, Ta; Y2 = Mo, W, Hf, Zr; Z2 = C, B, Si; and RE = rare earth elements. Ti-43.5Al-4Nb-1Mo-0.1B (TNM), which entered service in 2016 through the Pratt & Whitney PurePower™ geared turbo fan engine LPT forged blade, is a third generation alloy with enhanced performance compared to the second generation 4822. A refined as-cast grain size due to trace B additions and a higher volume fraction of high-temperature β -TiAl (disordered body centered cubic structure) phase due to balanced amounts of Nb and Mo impart

enhanced hot workability [3,4]. The ability to minimize volume fraction of β -TiAl (ordered B2 structure) phase via post-forging heat treatment provides balanced properties for TNM at room and service temperatures.

Coarse-grained lamellar microstructures exhibit relatively high fracture toughness and creep resistance, but poor tensile ductility, especially at room temperature. Fine-grained duplex microstructures exhibit low fracture toughness and creep resistance but moderate tensile ductility at ambient temperatures. This inverse correlation between tensile properties and resistance to fracture requires a careful selection of the microstructure for achieving balanced engineering properties [1,2,5,6]. Previous studies on γ -TiAl have shown that the fatigue crack growth rate da/dN and threshold level ΔK_{th} are dependent on the fabrication method and resulting microstructure [7–11]. Studies have also suggested that crack closure can play a role in the variation of fatigue threshold behavior and load ratio, R . Decreasing the lamellar spacing decreases the creep rate while increasing the fatigue crack growth resistance and ductility. It is empirically known that an increase of grain size or colony size increases the fracture toughness at the expense of fracture strain in tension [12]. The β phase surrounding α_2/γ lamellae significantly impacts the fracture properties [7] by providing a preferential fracture initiation and growth path due to its brittle nature.

While a two phase ($\gamma + \alpha_2$) alloy with a fully lamellar microstructure

* Corresponding author.

E-mail address: mxd394@case.edu (M.S. Dahar).

<http://dx.doi.org/10.1016/j.intermet.2017.08.015>

Received 3 May 2017; Received in revised form 19 July 2017; Accepted 22 August 2017

Available online 17 September 2017

0966-9795/ © 2017 Elsevier Ltd. All rights reserved.

Table 1
Chemical compositions (in at. %) of program materials.

Alloy	Al	Cr	Nb	Mo	B	C	O	Ti
4822	48	2	2			0.030	0.190	bal
TNM	43.56		4.05	0.97	0.1	0.008	0.061	bal

is used only in cast product form of 4822, a three phase ($\gamma + \alpha_2 + \beta/\beta_0$) TNM alloy is used in forged product form with greater microstructural flexibility. In both alloys, the as-cast microstructure is the foundation for final product microstructure that significantly influences the performance. Prior work by the present co-authors on as-cast 4822 demonstrated that R and orientation significantly influence da/dN and fracture behavior [13]. A strong dependence of da/dN upon the applied stress-intensity range ΔK was reported and Paris law slope m values greater than 10 were observed [13]. High m values significantly reduce the predicted component life and require the applied ΔK levels to remain below the fatigue threshold ΔK_{th} in order to prevent significant fatigue crack growth and/or failure. The objective of the present study is to address the following questions:

- Does a refined microstructure in as-cast TNM change the fatigue crack growth and fracture behavior compared to as-cast 4822?
- Does R and/or orientation influence fatigue crack growth parameters in as-cast TNM?
- Does the β phase in as-cast TNM affect the fatigue crack growth and fracture behavior?

Micro-mechanistic understanding of fatigue crack growth and fracture behavior was obtained based on test data generated on production-quality materials at various R values and orientations with respect to the casting direction, corroborated with extensive metallography and fractography, and plastic zone size analysis.

2. Program materials and experimental procedures

2.1. Materials

Second and third generation gamma TiAl alloys with nominal chemical compositions (in atomic percent) of Ti-48Al-2Cr-2Nb (4822) and Ti-43.5Al-4Nb-1Mo-0.1B (TNM) were investigated in this study. Complete chemical compositions are given in Table 1. The 4822 was cast at GE Global Research Center, Schenectady, NY to a geometry shown in Fig. 1. The rib and gate were removed to obtain a 100-mm long rectangular plate of 50-mm width \times 9.5-mm thickness. These plates were bisected along the length via electric discharge machining (EDM) to obtain two 25-mm width bend bars. Notches were placed to enable cracks to propagate in the L - T and T - L orientations. The TNM alloy was cast into a 50.8 mm diameter \times 3353 mm long ingot at Arconic Titanium and Engineered products, Niles, OH. Bend bars in the L - T and T - L directions were excised from this ingot as shown in Fig. 1.

The microstructures (optical and SEM) of as-cast 4822 and TNM program materials at different length scales are compared in Fig. 2. The average ($\gamma + \alpha_2$) colony size (determined by linear intercept method) of 4822 was $1000 \mu\text{m} \pm 144 \mu\text{m}$ and γ lath width was $1.77 \pm 0.5 \mu\text{m}$. TNM microstructure consisted of: lamellar ($\gamma + \alpha_2$) colonies in the 20–40 μm size range, γ lath widths of $\sim 0.2 \mu\text{m}$, and β of $\sim 9 \text{ vol } \%$ at grain/colony boundaries (determined using image analysis software MIPAR [14]).

2.2. Mechanical testing and characterization

Fracture toughness and fatigue crack growth rate tests were conducted on single-edge-notched and fatigue pre-cracked bend bar specimens prepared in accordance with ASTM standard E399 [15] and E647 [16]. Notches were placed using a slow speed diamond wire saw with a radius of 100 μm . Within the constraints of available cast article

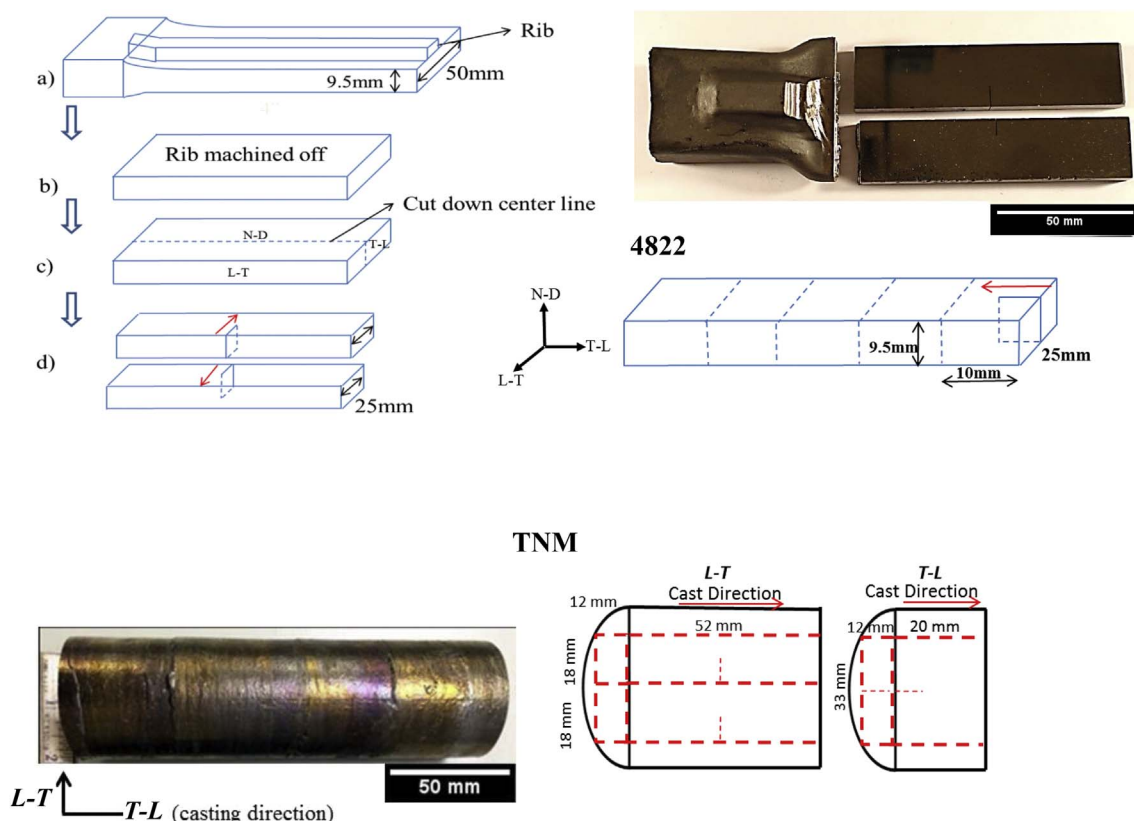


Fig. 1. As-cast 4822 (top) and TNM (bottom) test specimens extraction plans in L - T and T - L orientations.

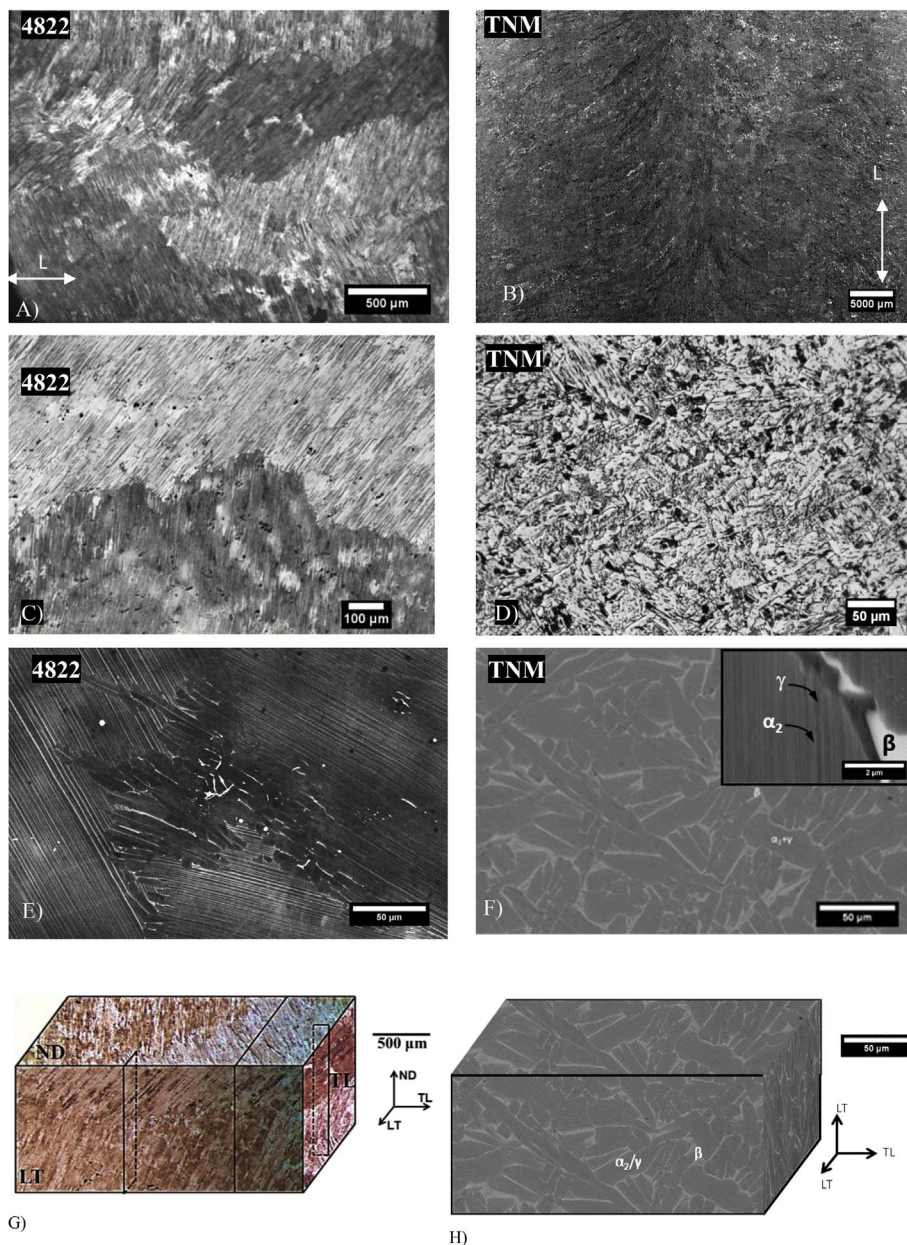


Fig. 2. Microstructures of as-cast 4822 (left) and TNM (right) program materials: A) 4822 optical macrograph, B) TNM optical macrograph, C) 4822 optical micrograph, D) TNM optical micrograph, E) 4822 backscattered electron image F) TNM backscattered electron image. G) 3D 4822 optical micrographs, and H) TNM 3D backscatter electron image. Optical micrographs were obtained on samples etched with Kroll's reagent. Phase contrast in backscattered electron images is: γ -grey, α_2 -dark, and β - bright.

sizes, duplicate bend bars with the following dimensions satisfying ASTM E399 were prepared to probe representative microstructure volumes: 4822 *L-T* samples of 100 mm \times 9.5 mm \times 25 mm, 4822 *T-L* samples of 25 mm \times 9.5 mm \times 12 mm, TNM *L-T* samples of 50 mm \times 20 mm \times 12.5 mm, and TNM *T-L* samples of 35 mm \times 20 mm \times 12.5 mm.

Fatigue crack growth rate tests were performed at room temperature in laboratory air using a closed-loop servo-hydraulic testing machine under cyclic stress-intensity (ΔK) control at a frequency of 20 Hz and at the load ratios, $R = K_{\min}/K_{\max}$, of 0.1, 0.3, 0.7, and 0.9. Crack growth rate was measured using direct current potential drop technique per ASTM E647 [16]. Fatigue threshold, ΔK_{th} , operationally defined as the applied ΔK below which $da/dN < 10^{-7}$ mm/cycle, was obtained by using a variable ΔK /constant- R load shedding scheme. Cyclic crack growth results are presented in terms of crack growth rate per cycle (da/dN) as a function of the applied stress intensity, $\Delta K = (K_{\max} - K_{\min})$. The test was started at a mid-range ΔK and used load-shedding to reach the threshold. The test was then stopped and restarted at a mid-range ΔK and the crack was grown to failure. After failure, the Paris slope m

and K_{\max} at failure were determined. Plane-strain fracture toughness tests were conducted on bend bars with notch length a in the range 0.45W–0.55W (W = specimen width) in accordance with ASTM E399 [15] on a span of 30-mm and at a displacement rate of 0.5 mm/min. Fracture surfaces were examined using a FEI Quanta 200 SEM at 20 kV. In addition, crack paths were analyzed using both optical and back-scattered electron imaging.

Tensile tests were performed on TNM using subscale tensile specimens with a double button head design and a gauge length of 20.3 mm conforming to ASTM E8 [17]. Tensile tests were performed at a strain rate of 10^{-3} s^{-1} and strain was measured using a non-contact video extensometer (from UVID™, LLC). Tensile tests were not performed on Ti4822 and lack of material prevented testing.

3. Results

Fatigue crack growth rate curves (da/dN vs ΔK) of both alloys in both *L-T* and *T-L* directions at $R = 0.1, 0.3, 0.7$, and 0.9 are presented in Fig. 3. Fatigue threshold ΔK_{th} , Paris slope m , and $K_c = K_{\max}$ at

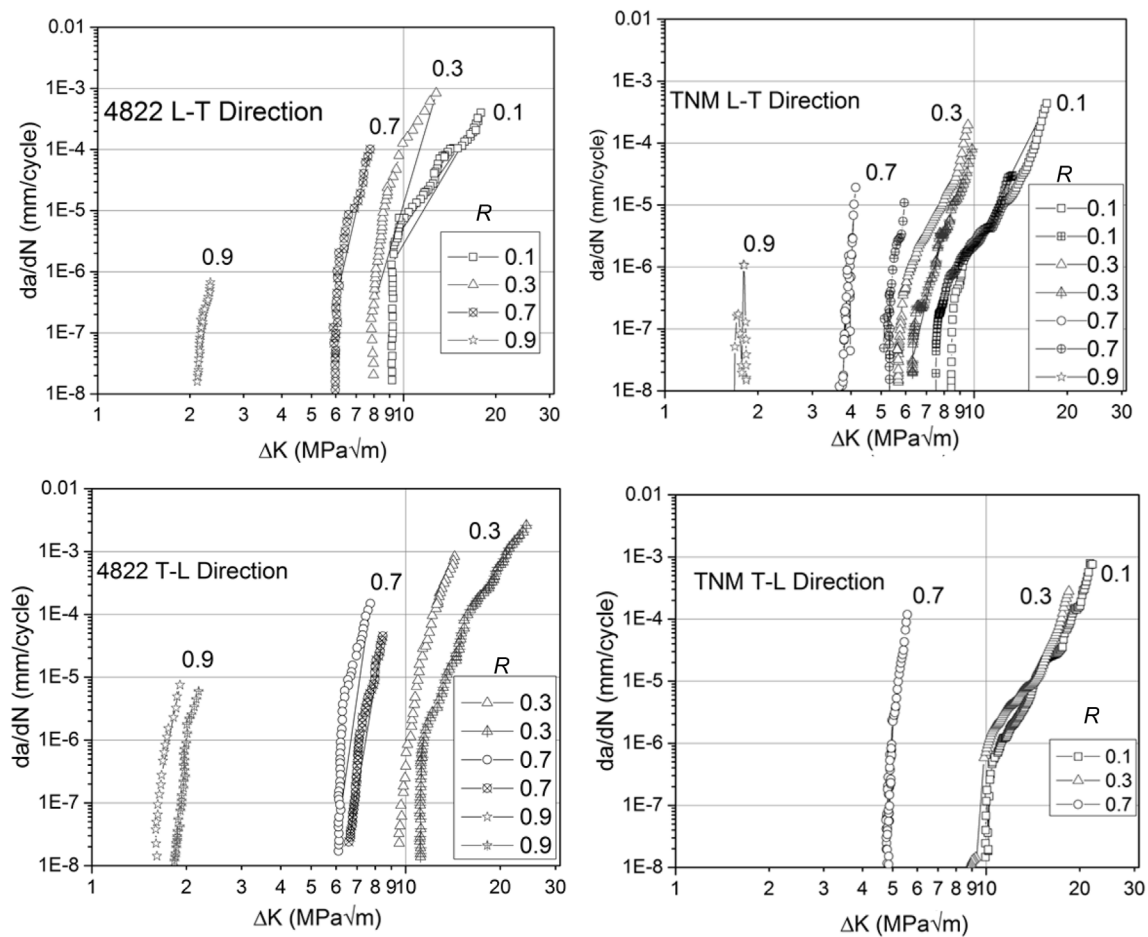


Fig. 3. Effect of load ratio R on fatigue crack growth rate curves of specimens tested in L - T direction (top) and T - L direction (bottom) of as-cast 4822 (left) and TNM (right).

overload at various R as well as static notch fracture toughness for both alloys in both orientations are summarized in Fig. 4. Both alloys exhibited decreasing ΔK_{th} with increasing R , Fig. 4 and Table 2. The influence of orientation on ΔK_{th} was more pronounced in TNM (compared to 4822), as evidenced by the rapid drop in ΔK_{th} with increasing R , and the absolute ΔK_{th} values at equivalent R were lower (Fig. 4 and Table 2). The ΔK_{th} at $R = 0.9$ for 4822 is significantly lower than that obtained at lower R , while increasing R shifted all of the da/dN - ΔK curves to the left. Paris slopes for both alloys in both orientations increased dramatically, from 9 at $R = 0.1$ to nearly 100 at $R = 0.9$. The K_c at failure in fatigue was not significantly affected by R , as seen in Fig. 4C. Tensile tests on TNM revealed a 0.2% yield strength of 680 MPa and ultimate tensile strength of 700 MPa with less than 0.5% plastic elongation.

Typical fatigue fractographs taken at different magnifications for 4822 and TNM tested in the L - T and T - L orientation are compared in Figs. 5 and 6. Both alloys exhibited brittle faceted failure features while the 4822 exhibited larger scale features compared to the TNM. Closer examination of the flat facets on the fracture surface in the Paris law regime revealed an absence of fatigue striations. High magnification fractographs at catastrophic overload in the fatigue tests and at various R and ΔK are shown in Fig. 7. Fracture surface features in both alloys were predominantly brittle with small amounts of local plastic deformation. The influence of ΔK or R on fractographic features is insignificant. Fig. 8 shows a comparison of 3D surface roughness profiles of fracture surfaces taken at intermediate ΔK over an area of $7 \times 7 \text{ mm}^2$ (taken with Keyence VHX-2000 microscope) for 4822 and TNM, both fatigue tested at $R = 0.3$ in T - L orientation. These show a surface roughness in the range of 800–1750 μm for 4822 and only 50–280 μm

for TNM. Fig. 9 shows a typical fractograph of TNM tensile tested specimens. Brittle fracture and surface roughness with singular features similar to those exhibited by the fatigue specimens are evident.

Crack path analysis was performed on polished and etched cross-sections of failed fatigue specimens. An example for a 4822 T - L sample fatigue tested to threshold at $R = 0.7$ is presented in Fig. 10. The crack path shows interlamellar and translamellar cracking that results from the propagation of the crack seeking the path of least resistance. The crack follows the colony boundaries and lamellae, causing the interlamellar and translamellar cracking along with some secondary cracking. Crack path for a TNM L - T sample tested to threshold at $R = 0.1$ presented in Fig. 11 shows microcrack propagation along β at colony boundaries, both along the crack path and subsurface. Cross-sections of the failed fatigue specimens in the L - T direction at $R = 0.7$ were mounted and polished to show the crack path on one side of the specimens as shown in Fig. 12. The cross sections confirms what was seen in previous crack path analysis.

4. Discussion

The fatigue crack growth data reveals a significant effect of R on the magnitude of the ΔK_{th} for 4822, decreasing from over 9 $\text{MPa}\sqrt{\text{m}}$ for $R = 0.1$ to less than 2 $\text{MPa}\sqrt{\text{m}}$ at $R = 0.9$. At a given R , the TNM shows a lower ΔK_{th} in both orientations compared to 4822. Crack closure can significantly impact the fatigue threshold and one key difference between the 4822 and TNM relates to the large differences in fracture surface roughness.

As discussed elsewhere [18], the roughness-induced crack closure arises due to the linkage of mismatched planes of deflected microcracks

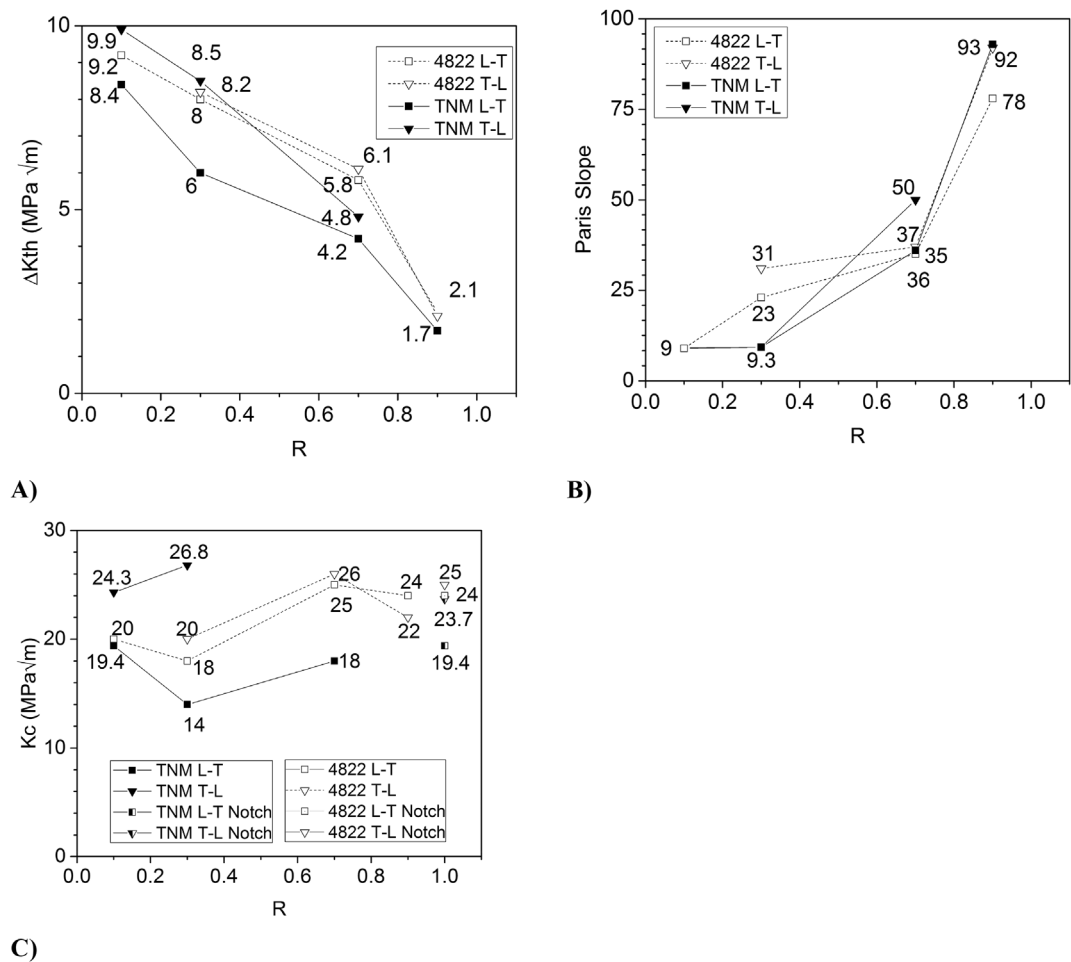


Fig. 4. Effect of load ratio R on A) fatigue threshold ΔK_{th} , B) Paris slope m , and C) K at overload failure K_c and notch toughness for 4822 and TNM in both L-T and T-L orientations.

Table 2
Cyclic plastic zone size of 4822 and TNM at threshold calculated with ΔK_{th} and K_{max} .

Orientation	R	ΔK_{th} (MPa \sqrt{m})		K_{max} at ΔK_{th} (MPa \sqrt{m})		Radius of Cyclic Plastic Zone (μm) at Threshold using ΔK		Radius of Monitonic Plastic Zone (μm) at Threshold using K_{max}	
		4822	TNM	4822	TNM	4822	TNM	4822	TNM
L-T	0.1	9.2	8.4, 7.5	10.2	9.3, 8.3	10.6	1.9, 1.5	52	9, 7
	0.3	8.0	6.3, 5.6	11.4	9, 8	8	1.1, 0.8	65	9, 7
	0.7	5.8	3.8, 5.4	19.5	12.6, 17.7	4.3	0.4, 0.8	174	17, 34
	0.9	2.2	1.7	21.5	17.8	0.6	0.1	212	34
T-L	0.1		9.9		11.1		2.7		13
	0.3	9.4	8.5	15.8	12.2	6.3	2	125	16
	0.7	6.0, 6.2	4.8	19, 20.9	16	4.5, 4.8	0.6	182, 216	28
	0.9	1.6, 1.8		16.1, 18.4		0.3, 0.4		131, 171	
Orientation	R	ΔK at overload (MPa \sqrt{m})		K_{max} at overload (MPa \sqrt{m})		Radius of Cyclic Plastic Zone (μm) at Overload using ΔK		Radius of Monotonic Plastic Zone (μm) at Overload using K_{max}	
		4822	TNM	4822	TNM	4822	TNM	4822	TNM
L-T	0.1	17.5	17.2, 13.2	19.4	19.1, 14.7	38.6	7.8, 4.7	190	39, 23
	0.3	8.9	9.8, 9.5	12.6	14, 13.6	9.9	2.6, 2.4	80	21, 20
	0.7	6.1	4.1, 5.9	20.2	13.8, 19.8	4.7	0.5, 1	208	21, 43
	0.9	2.2	1.8	22.4	18.3	0.6	0.1	253	36
T-L	0.1		21.9		24.4		13		64
	0.3	16.6	18.4	18.8	25	19.9	9.2	286	73
	0.7	6.2, 6.9	5.6	20.5, 23	18.7	6.0, 4.8	10.8	213, 270	37
	0.9	1.7, 2.2		16.8, 21.8		0.4, 0.6		143, 242	

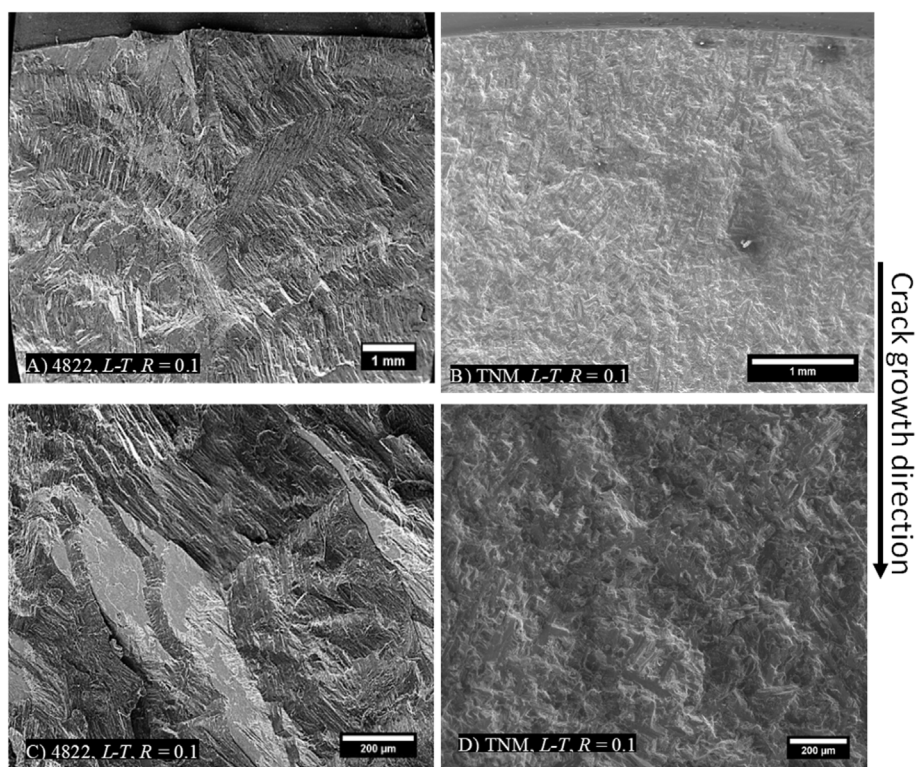


Fig. 5. SEM fractographs of fatigue specimen surfaces tested at $R = 0.1$ in the $L-T$ direction: A) 4822 overview, B) TNM overview, C) 4822 overload region, D) TNM overload region. Crack growth direction is from top to bottom.

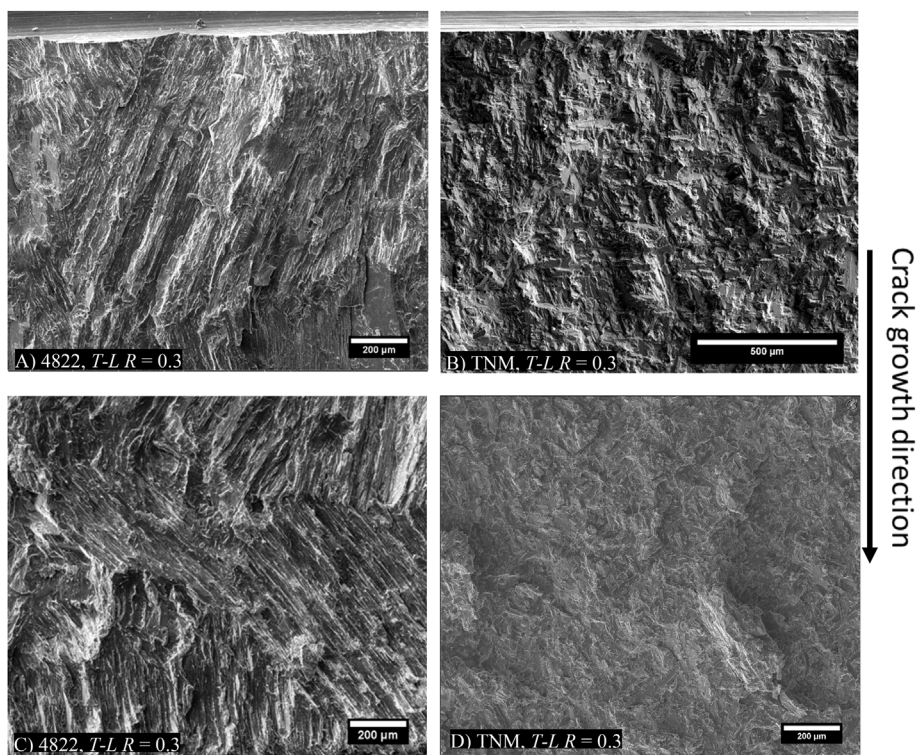


Fig. 6. SEM fractographs of fatigue specimen surfaces tested at $R = 0.3$ in the $T-L$ direction: A) 4822 overview, B) TNM overview, C) 4822 overload region, D) TNM overload region. Crack growth direction is from top to bottom.

via a process involving shear deformation and the fracture of thin ligaments. This has been postulated as the origin of roughness-induced closure observed in other Ti alloys and reported for TiAl alloys with large colony size similar to the 4822 in this study [19]. The higher fracture resistance exhibited by the lamellar microstructure is attributed to the deflected crack path which results in shear ligaments of large length and larger plastic dissipation contributed by the fracturing of the lamellar ligaments [5,18,20,21].

The irregular or rough fracture surfaces can induce high closure loads at low R when in-plane shear wedges open the crack at contact points along the crack face. The reduction in the effectiveness of this closure mechanism increases as the crack tip open displacement (CTOD) increases [22] and the crack faces are held apart.

The effect of changes in ΔK and K_{\max} in the fatigue cycle on the surface roughness can be estimated by determining the plastic zone size and examining how this compares to the microstructural features

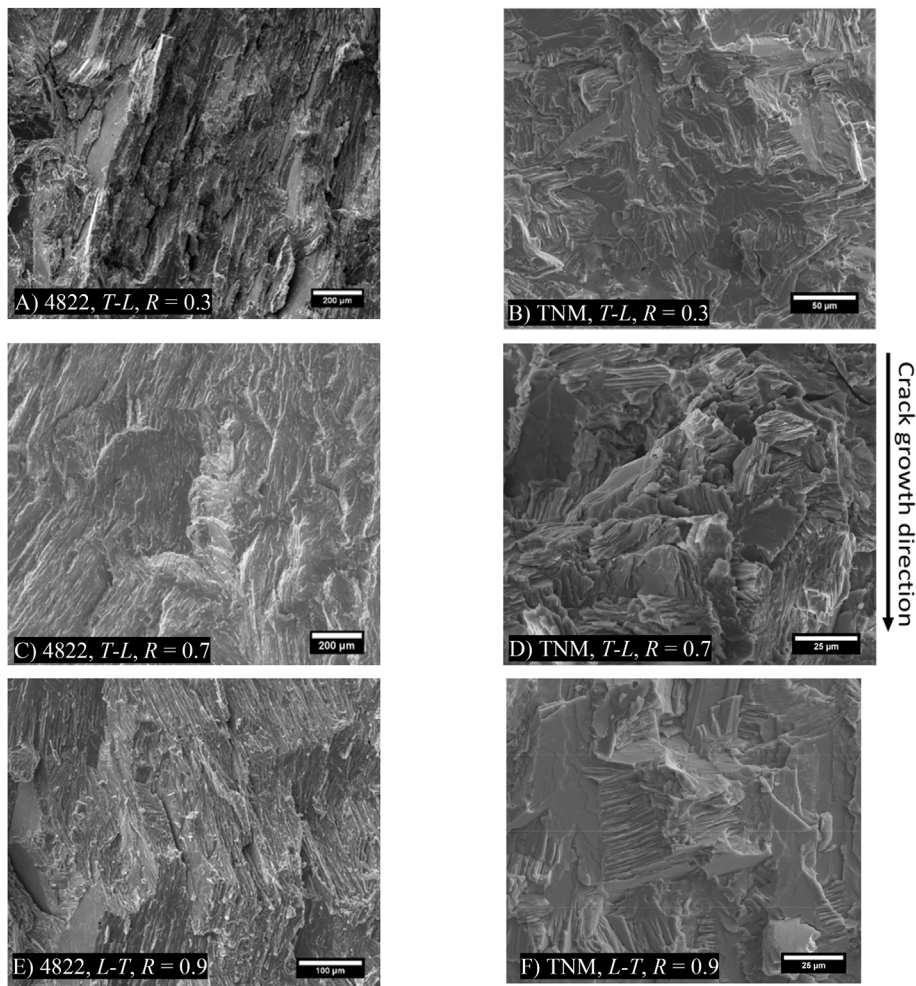


Fig. 7. SEM fractographs of specimens of specimens tested at different load ratios and at various ΔK : A) 4822, $T-L$, $R = 0.3$, rising ΔK , B) TNM, $T-L$, $R = 0.3$, rising ΔK , C) 4822, $T-L$, $R = 0.7$, at threshold, D) TNM, $T-L$, $R = 0.7$, at threshold, E) 4822, $L-T$, $R = 0.9$, rising ΔK , and F) TNM, $L-T$, $R = 0.9$, rising ΔK . Crack growth direction is from top to bottom.

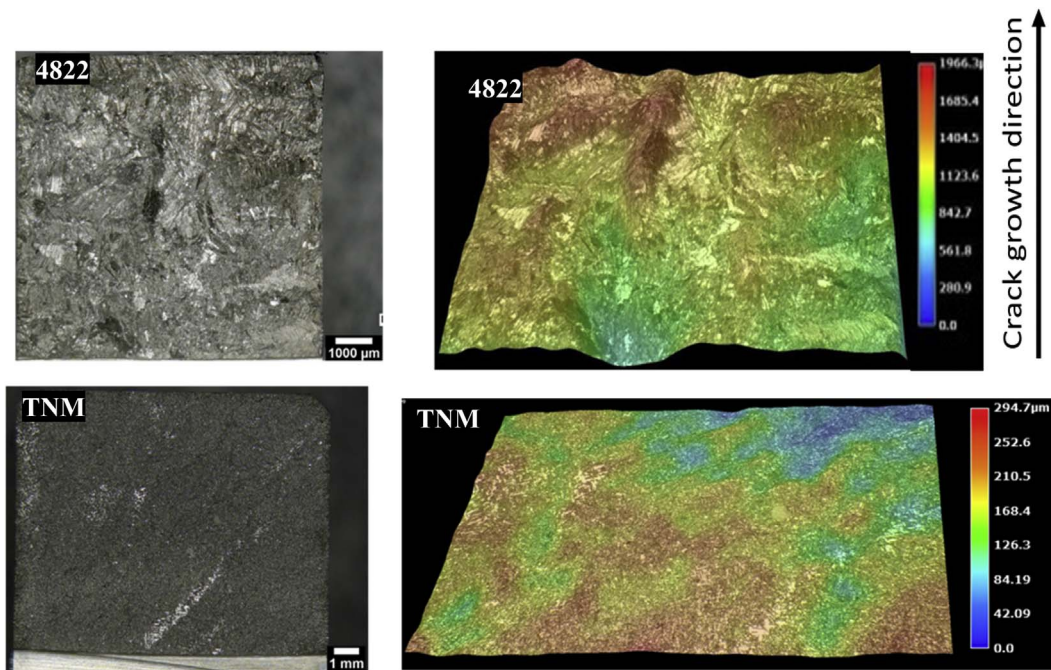


Fig. 8. 3D surface roughness plot of 4822 (top) and TNM (bottom) 7 mm \times 7 mm area taken at intermediate ΔK , both specimens fatigue tested in the $T-L$ direction at $R = 0.3$. For 4822, a peak of 1750 μm exists at the top left corner with troughs of 800 μm . The peak represents large roughness resulting from fatigue crack growth across a grain oriented in a different direction to adjacent grains. TNM sample exhibits a peak height of approximately 280 μm and troughs of 50 μm .

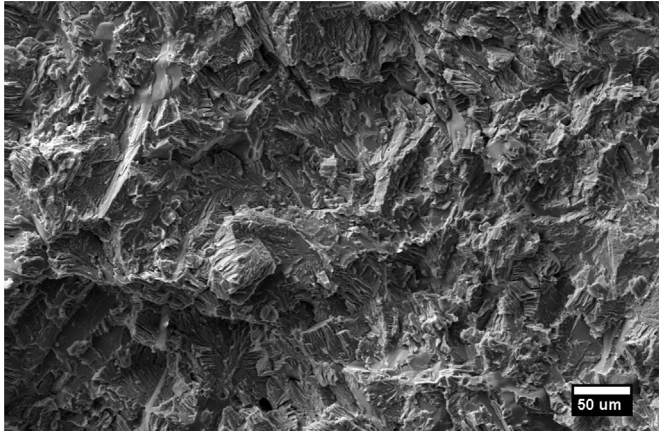


Fig. 9. SEM fractograph (backscattered electron imaging mode) of TNM tensile specimen (yield strength = 680 MPa, plastic elongation < 0.5%) showing mostly brittle faceted fracture.

sampled. The monotonic plastic zone radius in plane-strain is given by

$$r_{os} = \frac{1}{6\pi} \left[\frac{K}{\sigma_0} \right]^2 \quad (1)$$

where σ_0 is the yield strength of the material (342 MPa for 4822 and 680 MPa for TNM) [23]. The plastic zone size under cyclic loading will be smaller than that in static loading and is affected by reverse plasticity [23]. As the crack tip cycles during fatigue, the plastic zone leaves a wake of plasticity behind the crack tip. This induces residual stress in the crack tip region and may also play a role in crack closure. The cyclic plastic zone radius is given by

$$r_{oc} = \frac{1}{6\pi} \left[\frac{\Delta K}{2\sigma_0} \right]^2 \quad (2)$$

The calculated size of the monotonic and cyclic plastic zone at ΔK_{th} and overload for both 4822 and TNM ΔK and K_{max} are given in Table 2, assuming plain-strain conditions. The plastic zone size using K_{max} at threshold for the *T-L* test direction at $R = 0.3$ is 125 μm for 4822 which is considerably smaller than the colony size (~1000 μm). For TNM tested at $R = 0.3$, the plastic zone size at threshold using K_{max} is 16 μm, which is comparable to the colony size (~20–40 μm). Similar sizes are computed for other R values and orientations tested when using K_{max} . However, the cyclic plastic zone is considerably smaller than the colony size at the fatigue threshold for all of the R values and orientations tested, indicating that only a single colony is sampled in the plane of view, out of ~13 colonies of 4822 and 500 colonies of TNM sampled through the thickness. Thus, the orientation of only a few colonies dominates fatigue crack growth.

The cyclic plastic zone size at ΔK_{th} for 4822 is only on the order of the interlamellar spacing for all R values while the maximum plastic zone size is still only 1/5 to 1/10 of the colony size. The maximum plastic zone size still does not sample a full colony, suggesting that the drop in threshold with increasing R is from roughness-induced crack closure, consistent with the high surface roughness shown in Fig. 8. At overload, the plastic zone sizes at K_{max} are still at most only 1/5 of the colony size at all R values, thus sampling only a few colonies throughout the sample and producing similar values for K_{max} at failure.

For TNM, the cyclic plastic zone at threshold is on the order of the interlamellar spacing, while the maximum plastic zone size approaches the colony size. Thus, at high R values, the maximum plastic zone size will sample a full colony in the field of view and many through the sample thickness. However this will enable the crack to follow the brittle beta phase present on the colony boundaries and likely give rise

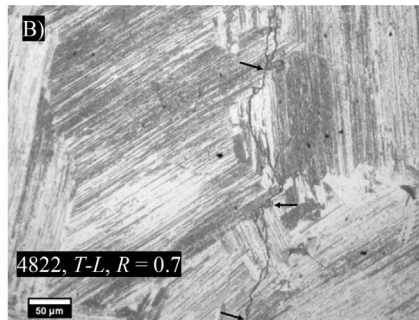
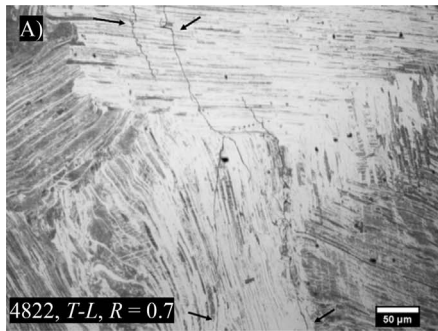
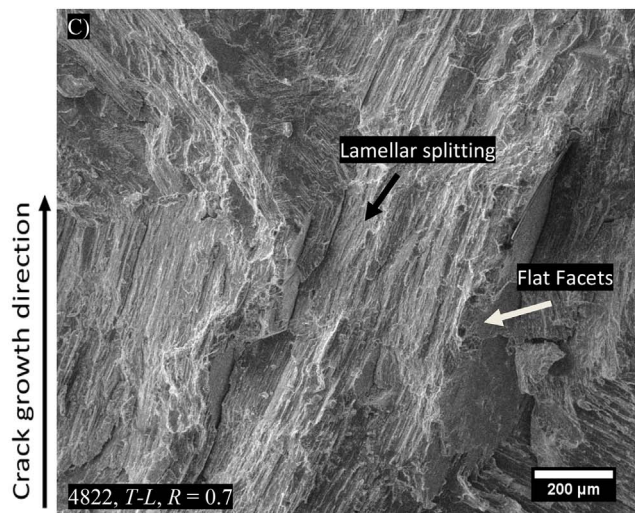


Fig. 10. Crack path in 4822 specimen fatigued tested in the *T-L* direction to threshold at $R = 0.7$. Crack growth direction is from bottom to top with arrows in A,B pointing to the crack path. Optical micrograph (etched with Kroll's reagent) showing A) translamellar and interlamellar cracks as well as secondary cracking, B) crack following a colony boundary, and C) secondary electron SEM fractograph in the overload region showing lamellar splitting (black arrow) and flat brittle facets (white arrow).



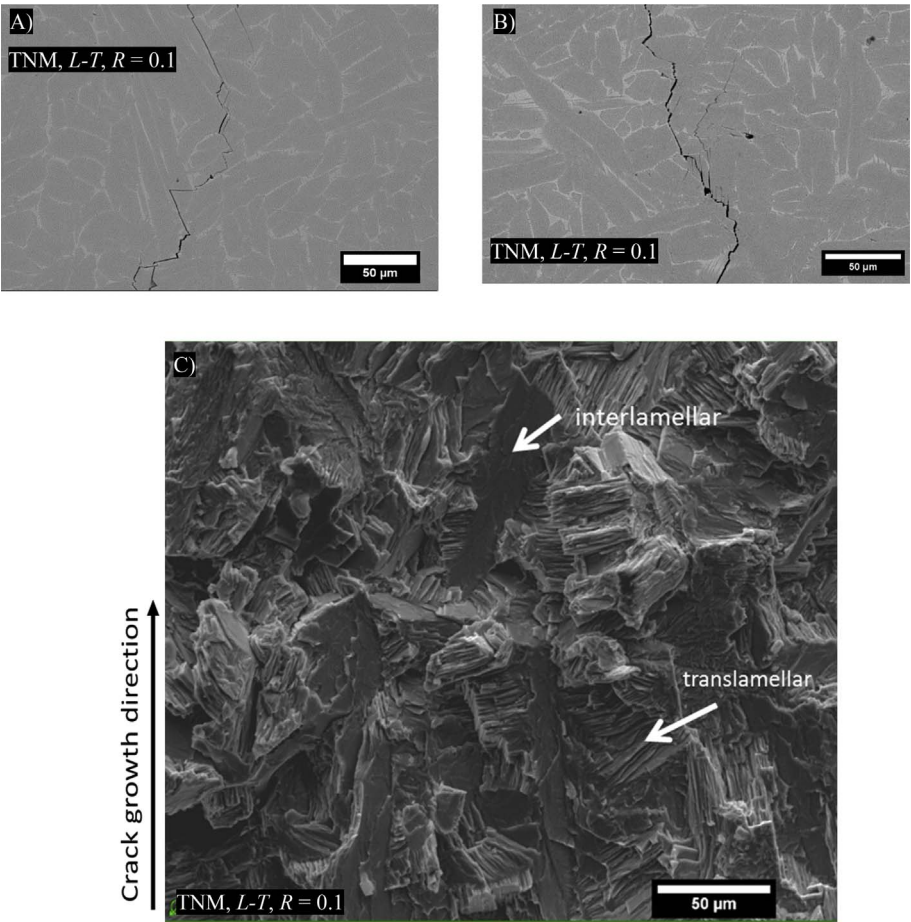


Fig. 11. Crack path of TNM specimen fatigue tested in the *L-T* direction to threshold at $R = 0.1$. Crack growth direction is from bottom to top. Backscattered electron images showing A) translamellar and interlamellar cracking with the crack following β at colony boundaries, B) secondary cracking and microcracking away from the crack path, and C) SEM fractograph in the medium ΔK region showing translamellar cracking with lamellar splitting and interlamellar fracture.

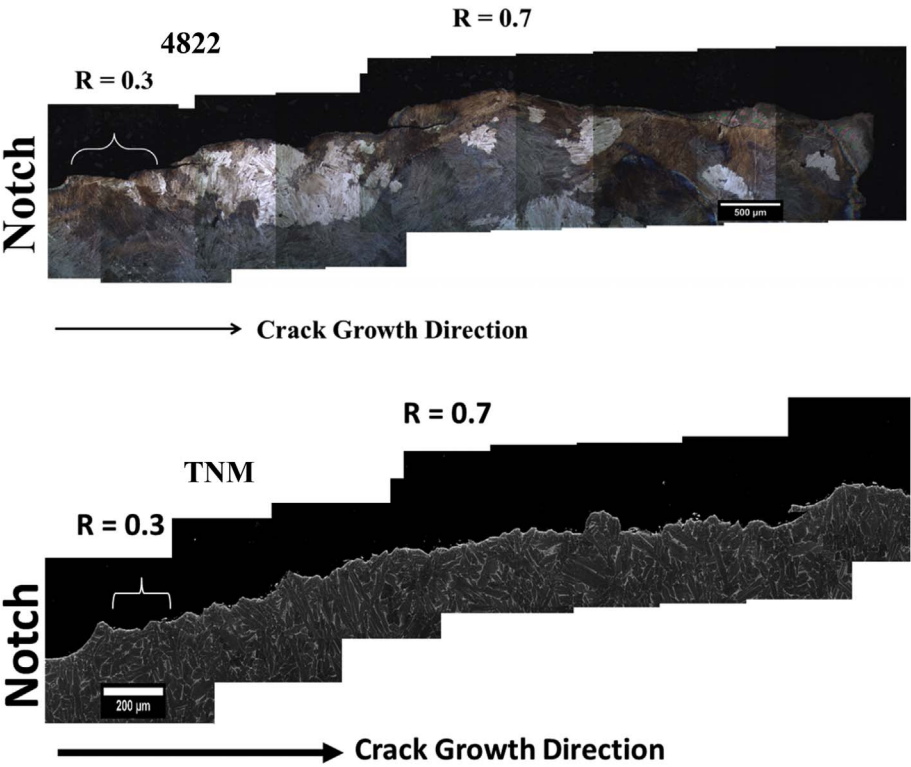


Fig. 12. (Top) Crack path of (optical) 4822 L-T broken sample fatigued at $R = 0.3$ and then $R = 0.7$. Secondary cracking is seen and the crack path follows the microstructure and produces significant roughness. (Bottom) Crack path of TNM (BSE) L-T broken sample fatigued at $R = 0.3$ and then $R = 0.7$.

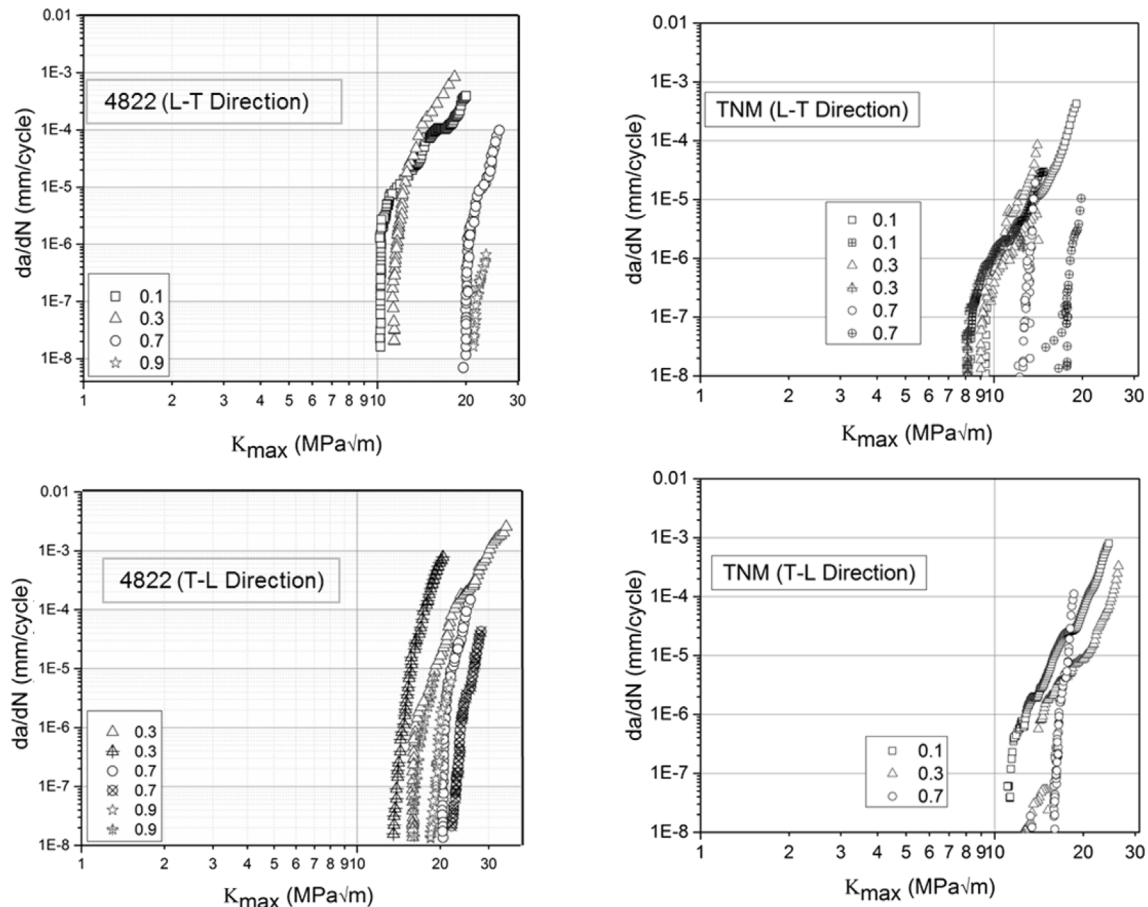


Fig. 13. K_{\max} vs. da/dN curves of 4822 (left) and TNM (right) tested in L-T (top) and T-L (bottom) directions at various R values.

to the large effects of R on the threshold. Since the surface roughness of the TNM samples, as seen in Fig. 8, is low, this limits any contribution from roughness-induced closure. At overload, the plastic zone sizes at K_{\max} are of the order of the colony size at all R values, easily sampling the brittle β regions on the colony boundaries throughout the sample thickness and producing similar values for K_{\max} at failure for all R values.

In order to begin to address the effects of microstructural features on the crack path as well as the R dependence of both ΔK_{th} and m , the fatigue crack growth data was first plotted as da/dN vs K_{\max} as shown in Fig. 13. The data for both 4822 and TNM do not completely collapse onto a single curve, suggesting an important, but not completely dominating effect of K_{\max} on the fatigue crack growth rate. In addition, m is ~ 9 at low R and approaches 100 at high R , again suggesting an important effect of K_{\max} on the crack growth rate. Furthermore, brittle modes of failure and absence of striations on the fatigue fracture surfaces support an important role of K_{\max} on the fatigue crack growth rate. For example, brittle fracture surface facets roughly $100 \mu\text{m}$ in size were exhibited by 4822. While these features are less than the colony size, they are in the range of the calculated plastic zone sizes and da/dN in certain regions, consistent with incremental crack growth of that size in certain regions of the fracture surface.

The data obtained on the 4822 and TNM exhibit characteristics that are similar to those exhibited by some metallic alloys [24–26] and intermetallics [13], with metallic-like Paris slopes in the range 3–5 at low R significantly increasing to > 10 with an increase in R . In these systems it has been shown that the increase in m with increasing R corresponds with an increase in static modes of brittle fracture that produce elevated crack growth rates that continue to increase with increasing R . In previous works [13,23–25], such static modes of

fracture included intergranular and cleavage failure. In the present work, the brittle fracture features in 4822 are likely to contribute to large increments in crack growth at a given ΔK , and are likely driven by K_{\max} as no fatigue striations were evident. In TNM, the crack path appears to be dominated by brittle β along colony boundaries, also providing a brittle crack path that should be dominated by K_{\max} and not ΔK . The continuous brittle β present around the lamellar colonies allow the crack, once initiated, to propagate unhindered. Once the crack reaches an end of a lamellar colony, the crack seeks a more favorable path, producing interlamellar and translamellar cracking. These fatigue crack growth mechanisms are similar to those reported by Leitner in TNM [7].

It must be noted that the present work was conducted on as-cast TNM material. Deformation processing is known to produce significant effects on the mechanical behavior of intermetallics due to various beneficial microstructure modification [27]. Studies are underway to understand the influence of deformation processing on fatigue and fracture behavior of TNM and the present work was conducted in order to provide a baseline understanding of the features affecting fatigue crack growth in the starting as-cast material.

5. Conclusions

The fatigue crack growth behavior of Ti-48Al-2Cr-2Nb (4822) and Ti-43.5Al-4Nb-1Mo-0.1B (TNM) in the as-cast condition were determined by testing over a range of R and stress intensity levels, in the L-T and T-L directions. Based on the observations of this investigation, the following conclusions were drawn.

- i) The as-cast 4822 had a large ($\gamma + \alpha_2$) colony size ($\sim 1000 \mu\text{m}$) and

- lath width of $\sim 1.77\ \mu\text{m}$ while the TNM had small colonies (20–40 μm) and fine lamellar spacing of $\sim 0.2\ \mu\text{m}$.
- ii) The fatigue fracture surfaces in both alloys in both orientations showed translamellar, interlamellar, and brittle fracture features. No fatigue striations were observed on the specimens tested in either orientation.
 - iii) The fatigue crack threshold was very dependent on load ratio. In particular, increasing the load ratio had a larger effect on reducing the fatigue threshold than reported for other TiAl materials.
 - iv) The fracture surface roughness quantified using confocal microscopy was large in 4822 (e.g. on the order of the colony size $\sim 1000\ \mu\text{m}$). In contrast, the surface roughness of TNM was considerably less but similarly on the order of the colony size (20–40 μm). The roughness of the surface in 4822 is produced by the cracks traversing the lamellar colonies causing interlamellar and translamellar cracking. These crack patterns were also found in previous studies on TiAl containing a lamellar structure, but the scale of roughness on the fracture was much greater in the 4822 than in other versions including TNM.
 - v) The Paris slope m for as-cast 4822 and TNM shows a large dependence on R , increasing from around 9 at $R = 0.1$ to over 90 at $R = 0.9$. Microstructural effects on the crack path were used to rationalize this observation.
 - vi) The fatigue threshold, Paris slope, fracture toughness, and notch toughness are not measurably affected by sample orientation and are similar for 4822 and TNM.

Acknowledgements

This work was supported by Arconic Titanium & Engineered Products with partial support provided by the CWRU Arthur P Armington Professorship. MD acknowledges Student Co-op support at Arconic Titanium & Engineered Products.

References

- [1] Y.-W. Kim, Ordered intermetallic alloys, part III: gamma titanium aluminides, *JOM* 46 (7) (1994) 30–39.
- [2] Y.-W. Kim, D.M. Dimiduk, Progress in the understanding of gamma titanium aluminides, *JOM* 43 (8) (Aug. 1991) 40–47.
- [3] H. Clemens, S. Mayer, Design, processing, microstructure, properties, and applications of advanced intermetallic TiAl alloys, *Adv. Eng. Mater.* 15 (4) (Apr. 2013) 191–215.
- [4] H. Clemens, S. Wilfried, V. Güther, and S. Mayer, Advanced intermetallic titanium aluminides. Ti-2015 Conference.
- [5] K.S. Chan, Y.-W. Kim, Influence of microstructure on crack-tip micromechanics and fracture behaviors of a two-phase TiAl alloy, *Metall. Trans. A* 23 (6) (1992) 1663–1677.
- [6] K.S. Chan, Toughening mechanisms in titanium aluminides, *Metall. Trans. A* 24 (3) (1993) 569–583.
- [7] T. Leitner, M. Schloffer, S. Mayer, J. Eßlinger, H. Clemens, R. Pippan, Fracture and R-curve behavior of an intermetallic β -stabilized TiAl alloy with different nearly lamellar microstructures, *Intermetallics* 53 (Oct. 2014) 1–9.
- [8] W.O. Soboyejo, P.B. Aswath, C. Mercer, Mechanisms of fatigue crack growth in Ti-48Al at ambient and elevated temperature, *Scr. Metall. Mater.* 33 (7) (1995) 1169–1176.
- [9] J.J. Kruzic, J.P. Campbell, R.O. Ritchie, On the fatigue behavior of γ -based titanium aluminides: role of small cracks, *Acta Mater.* 47 (3) (Feb. 1999) 801–816.
- [10] C. Mercer, J. Lou, W.O. Soboyejo, An investigation of fatigue crack growth in a cast lamellar Ti-48Al-2Cr-2Nb alloy, *Mater. Sci. Eng. A* 284 (1) (2000) 235–245.
- [11] C. Choi, H.J. Kim, Y.-T. Lee, Y.-W. Kim, C.S. Lee, Effects of microstructural parameters on the fatigue crack growth of fully lamellar γ -TiAl alloys, *Mater. Sci. Eng. A* 329–331 (Jun. 2002) 545–556.
- [12] K.S. Chan, Y.-W. Kim, Effects of lamellae spacing and colony size on the fracture resistance of a fully-lamellar TiAl alloy, *Acta Metall. Mater.* 43 (2) (Feb. 1995) 439–451.
- [13] M.S. Dahar, S.M. Seifi, B.P. Bewlay, J.J. Lewandowski, Effects of test orientation on fracture and fatigue crack growth behavior of third generation as-cast Ti-48Al-2Nb-2Cr, *Intermetallics* 57 (Feb. 2015) 73–82.
- [14] Powerful Image Analysis, MIPAR. [Online]. Available from: <http://www.mipar.us/> (Accessed: 14 February 2017).
- [15] ASTM Standard E399, Test Method for Linear-Elastic Plane-Strain Fracture Toughness K_{Ic} of Metallic Materials, ASTM International, 2009.
- [16] ASTM Standard E647, Standard Test Method for Measurement of Fatigue Crack Growth Rates, ASTM International, 2011.
- [17] ASTM Standard E8, ASTM E8/E8M-16a Standard Test Methods for Tension Testing of Metallic Materials, ASTM International, West Conshohocken, PA, 2016.
- [18] K.S. Chan, Micromechanics of shear ligament toughening, *Metall. Trans. A* 22 (9) (1991) 2021–2029.
- [19] K.S. Chan, Understanding fracture toughness in gamma TiAl, *JOM* 44 (5) (1992) 30–38.
- [20] K.S. Chan, Y.-W. Kim, Fracture processes in a two-phase gamma titanium aluminide alloy, in: Y.-W. Kim, R.R. Boyer (Eds.), *Microstructure/property Relationships in Titanium Aluminides and Alloys*, TMS, Warrendale, Pa, 1991, pp. 179–196.
- [21] S. Kampe, Microstructure morphology effects on fracture toughness of a cast near-gamma titanium aluminide alloy, in: Y.-W. Kim, R.R. Boyer (Eds.), *Microstructure/property Relationships in Titanium Aluminides and Alloys*, TMS, Warrendale, Pa, 1991, pp. 313–322.
- [22] R.O. Ritchie, S. Suresh, Some considerations on fatigue crack closure at near-threshold stress intensities due to fracture surface morphology, *Metall. Trans. A* 13 (5) (May 1982) 937–940.
- [23] N.E. Dowling, *Mechanical Behavior of Materials*, third ed., Oearson Pretice Hall, Upper Saddle River, NJ, 2007.
- [24] R.O. Ritchie, J.F. Knott, Mechanisms of fatigue crack growth in low alloy steel, *Acta Metall.* 21 (5) (May 1973) 639–648.
- [25] A.B. El-Shabasy, J.J. Lewandowski, Effects of load ratio, R , and test temperature on fatigue crack growth of fully pearlitic eutectoid steel (fatigue crack growth of pearlitic steel), *Int. J. Fatigue* 26 (3) (Mar. 2004) 305–309.
- [26] R.O. Ritchie, Mechanisms of fatigue crack propagation in metals, ceramics and composites: role of crack tip shielding, *Mater. Sci. Eng. A* 103 (1) (1988) 15–28.
- [27] M.G. Mendiratta, J.J. Lewandowski, D.M. Dimiduk, Strength and ductile-phase toughening in the two-phase Nb/Nb5Si3 alloys, *Metall. Trans. A* 22 (7) (1991) 1573–1583.